Exp Fluids (2017) 58:16
DOI 10.1007/s00348-016-2297-3

RESEARCH ARTICLE

Three-dimensional microscopic light field particle image velocimetry

Tadd T. Truscott[1] · Jesse Belden[2] · Rui Ni[3] · Jonathon Pendlebury[4] · Bryce McEwen[4]

Received: 4 March 2016 / Revised: 9 November 2016 / Accepted: 22 December 2016 / Published online: 11 February 2017
© Springer-Verlag Berlin Heidelberg 2017

Abstract A microscopic particle image velocimetry (μPIV) technique is developed based on light field microscopy and is applied to flow through a microchannel containing a backward-facing step. The only hardware difference from a conventional μPIV setup is the placement of a microlens array at the intermediate image plane of the microscope. The method combines this optical hardware alteration with post-capture computation to enable 3D reconstruction of particle fields. From these particle fields, we measure three-component velocity fields, but find that accurate velocity measurements are limited to the two in-plane components at discrete depths through the volume (i.e., 2C-3D). Results are compared with a computational fluid dynamics simulation.

1 Introduction

Advances in microfabrication processes have led to increased development of microfluidic devices in several areas, most notably in the biomedical field. The ability to obtain experimental measurements of flow properties in microfluidic devices is essential for validating numerical models, designing new devices, and improving existing designs. Time-resolved, three-dimensional velocity components can provide important, detailed information about flow field properties. One minimally intrusive method for measuring the velocity components of a flow field is particle image velocimetry (PIV). Originally, PIV was used as a means of effectively measuring two-dimensional flow fields. Improvements in digital imaging and computational capabilities have led to the development of methods capable of measuring all three components (3C) of velocities of particles in three-dimensional space (3D). Often, these methods are relatively complex, time-intensive and scarcely seeded. Micro-scale 3D-PIV (3D μPIV) methods have further complications and limitations due to size constraints and lighting difficulties. Some current 3D μPIV methods include confocal (Park et al. 2004; Lima et al. 2007), stereoscopic (Lindken et al. 2006; Bown et al. 2006), defocusing (Yoon and Kim 2006; Tien et al. 2008), volumetric correlation (Fouras et al. 2009) and holographic μPIV (Sheng et al. 2006). Depending on the requirements of the measurement, the attributes of one technique may be favored over another as there is no "one size fits all" system. A more comprehensive review can be found in Cierpka and Kaehler (2012). Here, we develop a low-cost easy-to-use light field (LF) μPIV method capable of resolving 3D particle distributions and 2C-3D μPIV measurements.

Development of novel and existing 3D μPIV systems continues to be an active area of research (Lindken et al. 2009). Confocal laser scanning microscopy (CLSM) uses hardware to produce high-contrast images at different focal planes (Park et al. 2004; Lima et al. 2007). Applying conventional PIV to the images yields two-component velocity vectors in planes perpendicular to the optical axis of the microscope (i.e., 2C-3D velocity fields). The method does not instantaneously measure 3D velocity vectors. Lindken et al. (2006) present a method for obtaining three-component velocity vectors from two-dimensional planes (3C-3D) using stereoscopic μPIV. Two cameras are used to

✉ Tadd T. Truscott
taddtruscott@gmail.com

[1] Utah State University, ENGR 419J, Logan, UT 84322-4130, USA

[2] Naval Undersea Warfare Center, Newport, RI, USA

[3] Pennsylvania State University, State College, PA, USA

[4] Brigham Young University, Provo, UT, USA

simultaneously capture images at different viewing angles and measurements are made along several planes in the z dimension to get velocity vectors throughout the entire flow field. They report that one of the limitations of stereoscopic μPIV is a decreased resolution along the optical axis (z direction) due to a large depth of focus of the stereoscopic objective lenses. Alternatively, a single camera 2C-3D method based on volumetric correlation was demonstrated by Fouras et al. (2009).

A method for obtaining three-dimensional, three-component (3C-3D) flow velocities in a microvolume based on the macroscale defocusing digital PIV method (Pereira et al. 2000) was presented by Yoon and Kim (2006). By placing a mask of three pinholes, arranged in an equilateral triangle configuration, between the objective lens and image plane, the depth of the particles could be correlated by the size of the resulting triangle pattern observed. In this method, particle seeding must be low because the triangle pattern becomes less distinguishable with increasing particle concentration. Light intensity is also a challenge because light transmission is limited by the pinhole mask. Tien et al. (2008) modified the setup to reduce this limitation using a color camera and color filters over each of the pinholes effectively making each color channel a separate image sensor. This method was refined to, instead, use three different colored light sources at different angles to produce the triangular patterns (Tien et al. 2014; Pereira et al. 2007). The 3D locations of particles are computed and velocities found using particle tracking velocimetry (PTV); the authors demonstrated the ability to instantaneously resolve unsteady velocity fields.

Wavefront sensing and astigmatism PTV (Chen et al. 2009; Cierpka et al. 2010) are similar techniques that use a cylindrical lens to generate an anamorphic image set where out-of-focus particles deform by different amounts in different directions. The difference in deformation can be correlated to the axial location of the particles. Another approach for 3D μPIV/PTV is digital holography, which records light interference patterns as a hologram and reconstructs the 3D field through post- processing (Sheng et al. 2006; Ooms et al. 2009). By finding the movement of particles from two time steps, the velocity field is generated.

Increasingly, concepts from light field imaging and computational photography are being exploited to make fluid measurements. As described by Levoy (2006), light field (LF) imaging attempts to measure the radiance of light along many rays that intersect a scene. This enables post-capture computational photography operations, such as the ability to refocus a scene at different depths thereby generating a focal stack of images that span a 3D volume. On the macroscopic scale, one of the more prevalent 3D PIV methods is tomographic PIV (Tomo-PIV) (Elsinga et al. 2006; Kim et al. 2011, 2012). Multiple synchronized cameras view an entire measurement volume from different angles and 3D particle fields are reconstructed using optical tomography to obtain instantaneous, 3C-3D velocity measurements. Belden et al. (2010) present a similar method that uses the concepts of LF imaging and synthetic aperture refocusing known as synthetic aperture particle image velocimetry (SAPIV). Images from an array of cameras are combined using an SA refocusing algorithm to generate a focal stack of narrowly focused synthetic images. The 3D particle field can be reconstructed by either thresholding the focal stack (Belden et al. 2010) or performing 3D deconvolution (Belden et al. 2014) and the seeding concentration can be large.

An alternative means of sampling a light field is to insert a microlens array between the main lens and image sensor of an imaging system, so as to measure ray radiance and angle (Ng et al. 2005). This approach introduces a trade-off of lateral resolution for angular resolution. A macro 3D PIV method using this so-called plenoptic camera was proposed by Lynch (2011, 2012). SA refocusing can be performed on plenoptic light field images as well, yielding a focal stack of synthetic images covering a 3D measurement volume.

Levoy et al. (2006) developed a method for converting a conventional microscope into a light field microscope. A microlens array is placed at the intermediate image plane between the objective and a camera. In this paper, microscopic LF imaging is employed to perform volumetric particle reconstructions and μPIV measurements. The use of a microlens array provides a practical and simple means of sampling ray radiance and direction on the microscale. Using SA refocusing and 3D deconvolution, we robustly reconstruct 3D particle fields. The seeding concentration is relatively large (e.g., 8 particles within a $24 \times 24 \times 8$ voxel interrogation volume), thus allowing velocity field computation via PIV. Measurements of velocity in a microchannel with a backward-facing step are compared with CFD. Limitations of the method arising from the trade-off between lateral and angular resolution are also discussed.

2 Light field micro-imaging

A four-dimensional light field written as $L(u, v, s, t)$ describes the radiance along all rays that intersect a scene as parameterized by the intersection of the rays with two planes (the uv and st planes) (Levoy and Hanrahan 1996). Placing an array of microlenses (lenslets) at the intermediate image plane of an imaging system (as shown schematically in Fig. 1) enables capture of a sampled version of a four-dimensional light field in a single photograph (Levoy et al. 2006; Ng et al. 2005). The microlenses define the st plane and the camera sensor defines the uv plane. A light

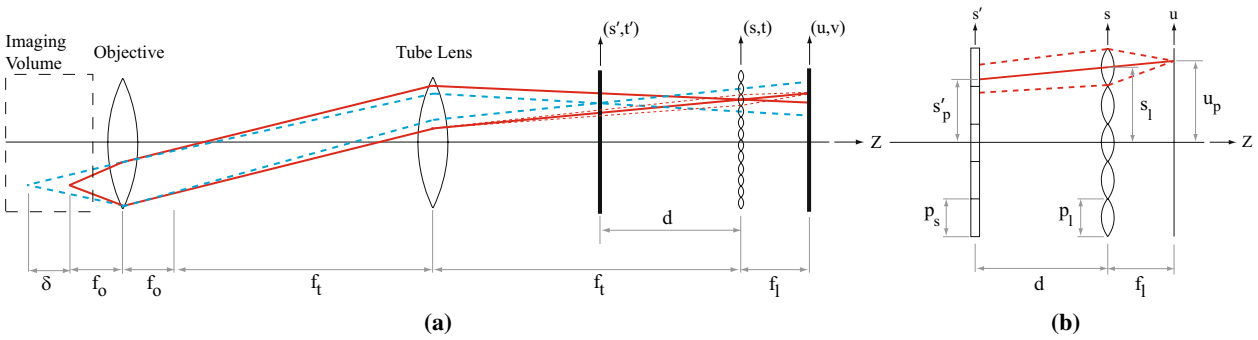

Fig. 1 **a** Ray diagram of a light field microscope that makes use of an infinity-corrected objective. An in-focus object projects to a point on the microlens plane (*red* rays), while rays from an out-of-focus point span multiple microlenses (*blue* rays); depth is, thus, encoded by the microlens array. **b** A synthetic image is formed on the $s't'$ plane by reprojecting pixels through their parent lenslets

field can be reparameterized to recover information in the depth (Z) dimension, which requires trading lateral spatial resolution for angular resolution (Ng et al. 2005). For a lenslet-based light field microscope, the spatial resolution is controlled by the size of the lenslets, while the depthwise (or axial) resolution is governed by the number of resolvable spots behind each lenslet (Levoy et al. 2006).

2.1 Synthetic refocusing

Figure 1 shows a schematic of a light field microscope in which a microlens array has been placed at the intermediate image plane of a microscope with an infinity-corrected objective. The sensor plane (uv) is placed behind the microlens plane at a distance equal to the lenslet focal length, f_l. Rays from a point on an in-focus object in the imaging volume (solid lines in Fig. 1a) meet at a point at the lenslet plane, and thus spread in a circular pattern (for a circular aperture) behind a single lenslet. Rays from a point in the imaging volume not at the focal depth (dashed lines in Fig. 1a) do not meet at a point at the lenslet plane and thus span multiple microlenses. Therefore, the depth information about this out-of-focus point is encoded in certain pixels behind more than one lenslet. A particular depth in the imaging volume can be brought into focus by reparameterizing the light field post-capture. In other words, the light can be reprojected to a new imaging plane (e.g., the $s't'$ plane) behind the tube lens, and a refocused image can be synthesized to effectively move the plane of focus of the microscope.

Refocused images are formed using geometry that assumes each lenslet acts as a pinhole. Therefore, each pixel is reprojected along the direction given by the vector connecting the pixel and the center of its parent lenslet. Thus, the first step in refocusing the light field involves pairing each pixel on the sensor (uv) plane with its parent lenslet by determining which pixels are behind each microlens on the st plane. Each pixel is then reprojected to the desired synthetic focal plane $s't'$ located at a distance d from the lenslet plane (note: d is positive if $s't'$ is to the right of st and negative if to the left of st). As depicted in Fig. 1c, the $s't'$ coordinates of a reprojected pixel can be found from similar triangles and are given by

$$\begin{bmatrix} s'_p \\ t'_p \end{bmatrix} = \frac{d}{f_l}\begin{bmatrix} u_p \\ v_p \end{bmatrix} + \left(1 - \frac{d}{f_l}\right)\begin{bmatrix} s_l \\ t_l \end{bmatrix} \tag{1}$$

where (u_p, v_p) are the coordinates of the pixel at the sensor plane and (s_l, t_l) are the coordinates of the parent lenslet center at the lenslet plane. The uv and st plane are assumed to have origins on the Z axis.

Refocusing on a synthetic image plane effectively moves the object plane of the microscope by a distance δ. For a general optical system, one would expect the magnification to change with a change in the image and object plane locations. However, for an infinity-corrected objective (as used herein), the total magnification is a constant and is given by $M = -f_t/f_o$, where f_t and f_o are the focal lengths of the tube lens and objective lens, respectively. It can then be shown (see "Appendix") that the new synthetic image plane and object plane displacements are related by:

$$\delta = \frac{d}{M^2} \tag{2}$$

A refocused image is formed at the $s't'$ plane by integrating all reprojected pixels over a discretized synthetic image plane. Because the magnification is constant, the spatial resolution of the discretized synthetic image plane should be the same for every new focal depth. Levoy et al. (2006) showed that the lateral spatial resolution of the light field equals the size of the lenslets, p_l. Therefore, we sample the discretized synthetic image plane with resolution $p_s = p_l$ and an overall size of $N_s \times N_t$, where N_s and N_t are the number of lenslets in the s and t dimensions, respectively.

A bilinear interpolation scheme is used to sample the synthetic images. It should be noted that by tracing the marginal rays from a given pixel (shown by the dashed lines in Fig. 1c), the area of intersection with the synthetic image plane will be smaller than the lenslet area because the rays converge to a point on the tube lens. However, to reduce computational complexity when sampling a new synthetic image, it is assumed that the light from a given pixel intersects the $s't'$ plane over an area equal to the lenslet area. Refocusing algorithms were implemented in Matlab and the code can be found online (SplashLab 2014).

The sacrifice in lateral resolution is made to gain angular resolution of the light rays, which can be exploited for resolution in the axial (i.e., depth, Z) dimension. The axial resolution of an LF microscope was derived by Levoy et al. (2006) and relevant aspects are presented here for context. The angular resolution is described by the number of resolvable spots behind each lenslet computed as:

$$N_u = \frac{p_l^2}{R_{\text{obj}}}, \tag{3}$$

where lenslets are assumed to have equal length p_l in the s and t dimensions. R_{obj} is the smallest resolvable distance between two points on a specimen imaged by a microscope and is given as

$$R_{\text{obj}} = \frac{0.47\lambda}{2\text{NA}}M, \tag{4}$$

where λ is the wavelength of light, NA is the numerical aperture of the objective and M is the magnification. The pixel pitch, p, of the image sensor must be less than p_l/N_u or the pixel size will limit the angular resolution. Levoy et al. (2006) define axial resolution in several ways, but most relevant for the present work is the depth of focus of synthetically refocused images, which is computed as

$$D_{\text{tot}_2} \approx \frac{(2+N_u)\lambda n}{2\text{NA}^2} \tag{5}$$

where n is the index of refraction of the medium in which the objective is immersed (herein, the medium is air, $n = 1$). Considering that N_u is the number of non-overlapping depths within an SA focal stack (Levoy et al. 2006), the expected total resolvable volume depth can be estimated as

$$D_V \approx N_u D_{\text{tot}_2} \tag{6}$$

To avoid under-sampling, it is common to generate more than N_u synthetic focal planes; therefore, the focal stacks used in this work are generated with depth spacing of

$$\delta_{\text{FP}} \approx \frac{D_{\text{tot}_2}}{3} \tag{7}$$

In μPIV applications, light rays experience a refractive index change as they pass from the working fluid in a microchannel into the medium surrounding the objective (air). The relationship between the synthetic image plane and the synthetic object plane displacement in Eq. 2 assumes that the object is in the same medium as the objective and must be corrected for this refractive index change. A reasonable approximation for the true object plane displacement (see Appendix for derivation) is given by

$$\delta' = \frac{n_f}{n}\delta \tag{8}$$

where δ is the apparent object depth and n_f is the refractive index of the working fluid. The apparent object depth is the object plane location that would occur with a uniform refractive index. Similarly, the depth of focus, total volume depth and focal plane spacing derived in Eqs. 5–7 are corrected by substituting D_{tot_2},D_V and δ_{FP} for δ in Eq. 8, respectively.

To demonstrate light field refocusing, a glass slide containing fluorescent particles was angled with respect to the optical axis and imaged without a microlens array at three different depths. A light field image of the slide was also captured and synthetically refocused at the three different depths. Figure 2a shows a raw light field microscope image of the glass slide. The top of the slide is farther from the microscope objective than the bottom. A laser (532 nm) illuminates the particles, which fluoresce at 560 nm. The focal plane is slightly above the center of the image. In Fig. 2b–d, the lenslet array has been removed from the microscope and the microscope lamp provides the illumination for the glass plate and particles. The focal plane locations are set by translating the objective to $Z = 68.5$, 0 and -73.5 µm for Fig. 2b–d, respectively. Figure 2e–g show the result of refocusing the light field image from Fig. 2a at depths nearly equal to those shown in Fig. 2b–d. Figure 2h–j shows the same focal planes after deconvolution. The refocused light field images match well with the conventional micrographs with some reduction in resolution.

2.2 3D deconvolution

The blurring effect evident in the refocused images in Fig. 2e–g would introduce significant noise into the PIV measurements if not removed. Fortunately, Levoy et al. (2006) showed that this blurring can be mitigated through a 3D deconvolution approach. We consider the synthetic focal stack to be a volume with spatial intensity $i(x, y, z)$. Under the assumptions of linearity and shift-invariance in formation of the 3D refocused volume, the formation process can be modeled as a 3D convolution (Levoy et al. 2006; Sibarita 2005) written as

$$i(x,y,z) = h(x,y,z) \otimes o(x,y,z), \tag{9}$$

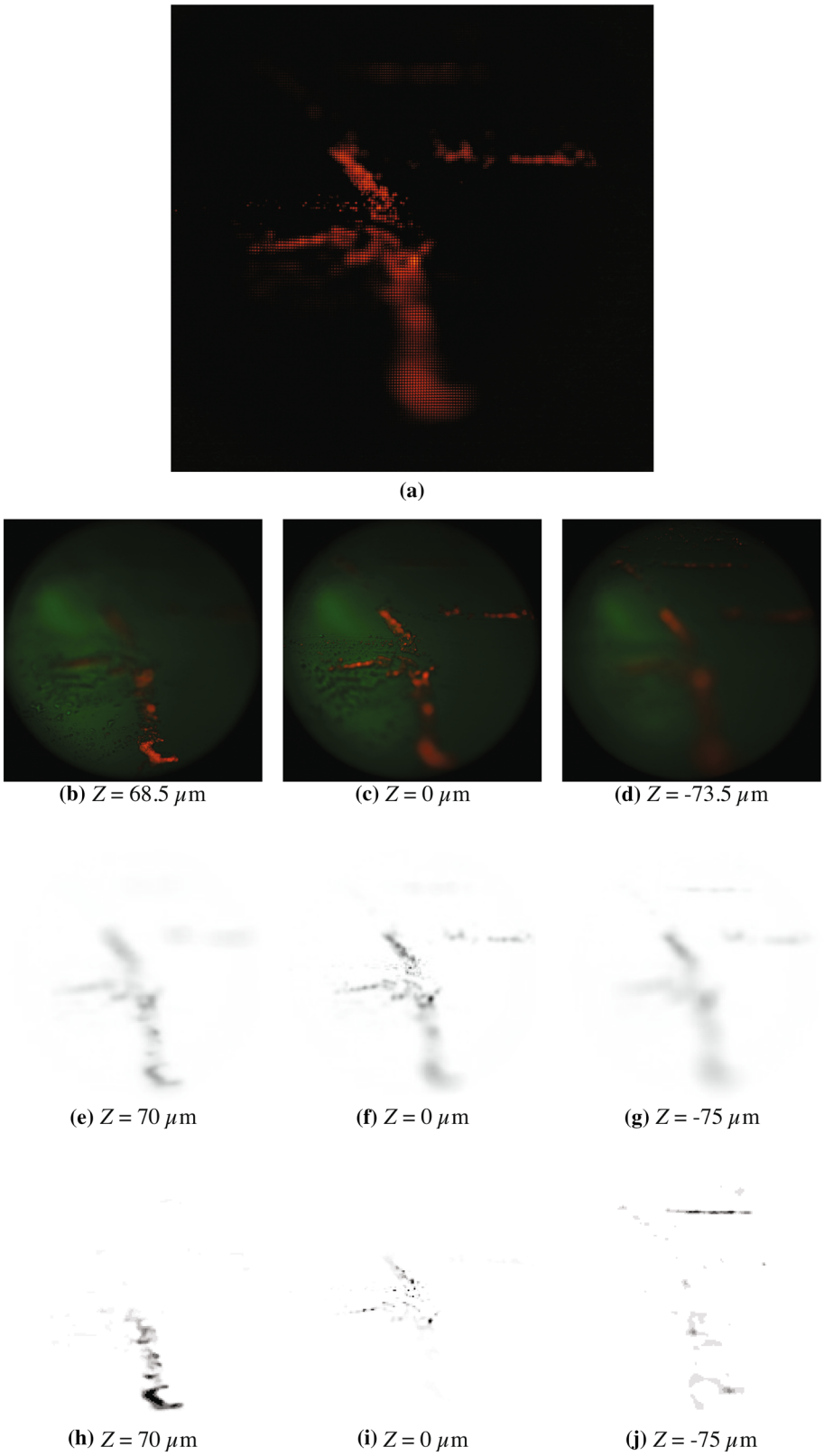

Fig. 2 Refocusing of a light field image of particles on a tilted slide. **a** Original, raw light field image. **b–d** Conventional microscope images without a microlens focused at three different depths as marked. **e–g** Light field images refocused at similar depths to **b–d** with inverted color mapping. **h–j** Light field focal planes corresponding to **e–g** following 3D deconvolution with inverted color mapping

where $o(x, y, z)$ is the true object and $h(x, y, z)$ the 3D point spread function (PSF) of the optical system. 3D deconvolution attempts to invert Eq. 9 to estimate o given i and an estimate of h (Sibarita 2005). Figure 3 shows a graphical representation of Eq. 9 where the slice from the deconvolved volume is an estimate of the true object. Regardless

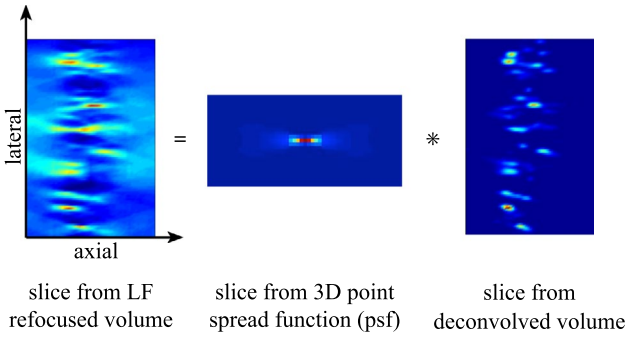

Fig. 3 Process of deconvolution. The image on the *left* shows a cross-section of the refocused light field and the middle image is a slice from the 3D point spread function (PSF) of the light field microscope system. An iterative deconvolution algorithm yields an estimate of the original object, a slice of which is shown in the *right image*

of the algorithm used to perform deconvolution, an accurate estimate of the PSF is essential. For light field microscopy, Levoy et al. (2006) recommend empirically estimating the PSF by imaging a sub-resolution fluorescent bead in the center of a lenslet and refocusing the light field, thus generating a focal stack of the PSF. Because it is critical to maintain the same optical characteristics for the PSF images as for the PIV experiment, it may not be practically feasible to image a sub-resolution bead in the center of a lenslet. Therefore, we form an estimate of the PSF by refocusing sparsely seeded light field PIV images, and averaging sub-volumes corresponding to several different particles. Although the particles are likely larger than is desirable, we have achieved good 3D deconvolution results.

Levoy et al. (2006) found that an iterative deconvolution algorithm is appropriate for volumes reconstructed with limited angular resolution, as is the case for light field imaging. In this work, the iterative Richardson–Lucy algorithm, commonly applied in traditional optical microscopy (Sibarita 2005), is used with 50 iterations. Figure 3 shows slices from the refocused volume, the average PSF and the estimated object obtained; images are from actual PIV microchannel data. The blurring that is very apparent in the refocused volume is largely removed in the deconvolved volume. Levoy et al. (2006) performed optical performance tests and observed that refocused images at locations far from the original focal plane, but still within the range over which the light field microscope could be refocused, were not as sharply focused and the cause was attributed to uncorrected spherical aberrations in the objective lens. In our system, this contributes to velocity measurement errors at the extreme depths of the volume. Finally, although the blurring artifacts are reduced through 3D deconvolution, the reconstructed particles are elongated in the axial dimension by a factor of ≈4. This is a result of the reduced axial resolution and has an effect on the PIV results as discussed in Sect. 4.

3 Experimental methods

3.1 Setup

A diagram of the experimental setup is shown in Fig. 4a. The light field microscope system consists of a Zeiss Axiovert 200 inverted microscope with an EC Plan-Neofluar 20x/(NA = 0.5) objective lens, a 21 Megapixel Canon EOS Mark II 5D DSLR camera (pixel pitch = 6.4 μm) with a 105-mm Nikon macro lens. A microlens array manufactured by Adaptive Optics Associates (cost ≈ $1000) consists of plano-convex lenses with a

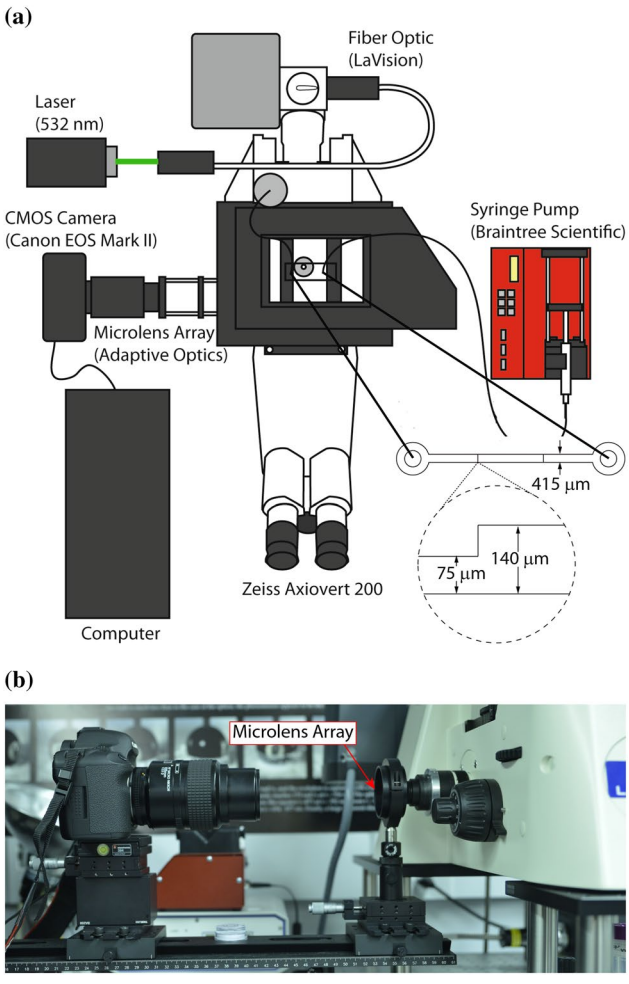

Fig. 4 **a** Experimental setup of the light field microscope and microchannel flow. **b** Image of the microlens array, which is placed at the intermediate image plane of the microscope. The back focal plane of the microlens array is imaged with a 1:1 DSLR camera

pitch of $p_l = 125\,\mu m$ and a focal length of $f_l = 2.5$ mm. Using Eqs. 3–6, we find that this light field arrangement gives $N_u = 12.5$ resolvable spots, $D_{\text{tot}_2} = 20.6\,\mu m$ and $D_V = 257\,\mu m$, where each length has been corrected for the refractive index change using Eq. 8 with $n_f = 1.333$ for water.

A collimated laser beam with a 532-nm wavelength reflects off of a dichroic mirror and passes through the objective lens, illuminating the tracer particles in the flow volume. The tracer particles are 1.7–2.2 μm Nile Red fluorescent spheres (Spherotech), which fluoresce above 550 nm. A filter allows only the higher wavelengths emitted from the fluorescent particles to pass, removing unwanted reflections of the laser light off of the channel walls, significantly increasing the signal-to-noise ratio. A syringe pump (Brain Tree Scientific, BS-300) drives a 1:5 solution of fluorescent particles to distilled water in a 25 μL syringe (Hamilton) through PVC micro-tubing (508 μm I.D.), where it connects though a micropipette tip to the PDMS microchannel containing a backward-facing step. Images are captured at the camera's maximum frame rate of 3.9 frames per second (internal triggering) with a 0.02-s exposure, and stored on a computer for processing. The low frame rate limits the maximum flow rates that can be measured in the channel. This limitation is imposed by the desire to have a large number of pixels to maximize lateral and axial resolution. Flow rates of 0.4 and 0.6 μL/min were imaged, which correspond to a Reynolds number of ≈0.02 and 0.03, respectively. Approximately 900 μm of the channel length in the flow direction is visible in the field of the view of the microscope. The backward-facing step is positioned in the middle of the field of view, with the flow-wise direction moving from the thin section into the thick section.

The geometry of the microchannels used in these experiments is shown in Fig. 4a. The width of the microchannel is 415 μm and the depth in the thin and thick sections is 75 and 145 μm, respectively. The channels are constructed from polydimethylsiloxane (Sylgard 184, PDMS). Photolithography is used to create a positive mold from SU-8 photoresist on a silicon wafer. PDMS is cast around the positive mold and cured in an oven at 90 °C for approximately 20 min. The channels are then cleaned with ethyl alcohol and bonded to a glass coverslip. The height of the channel at the mid-section and at the high section is measured using the focusing dial on the microscope, which has a resolution on the order of 1 μm. The microscope was focused on particles stuck to the base of the channel, then focused on particles stuck on other parts of the channel and the difference in position of the dial corresponded directly to the height of the channel.

3.2 Calibration method

Proper calibration of the light field microscope requires that the camera sensor lies on the focal plane of the lenslet array and that the lenslet array lies on the intermediate image plane of the microscope. Setting the correct distance between the camera sensor and the lenslet focal plane, f_l, is the most important part of calibration and is necessary for producing valid light field images. The following steps are performed to calibrate the system:

1. A slide with fluorescent particles is brought into focus in the eyepiece of the microscope.
2. The lenslet array is removed from the optics train so that the camera images the viewport directly. The camera is set in live mode and with the macro lens on the camera set to a magnification of 1:1, the camera is positioned such that the particles in the viewport are in focus in the camera. The particles should now be in focus in the microscope and the camera.
3. The lenslet array is returned to the optics train between the camera and the viewport (Fig. 4b) and positioned such that a grid pattern appears overlaid on the particle image. When the grid pattern appears, as seen in Fig. 5a, the microlens array plane is conjugate with the camera focal plane (Zhang 2010).
4. The lenslet array is adjusted until the micro lenses are vertically and horizontally aligned with the camera sensor.
5. The camera is moved back until it is conjugate with the focal plane of the lenslet array. When the camera is properly focused on the back focal plane of the lenslet array, each lenslet subimage will be nearly uniformly filled for objects that are in focus, as seen in Fig. 5b.
6. When all adjustments are complete, an image is captured of an in-focus white background illuminated by a mercury vapor lamp (Zeiss HBO 100) and used as a calibration image to define the (s, t) locations of the lenslet centers.
7. An image is taken of a single particle directly behind a single lenslet. This particle is used to generate the PSF used for deconvolution.

3.3 Particle volume reconstruction

Experimental light field images were refocused with a focal plane spacing $\delta'_{\text{FP}} = 6.21\,\mu m$ (corrected for index of refraction change using Eq. 8) over a range spanning beyond the top and bottom of the channel using the method described in Sect. 2.1. Based on the magnification of the objective ($M = 20$) and the microlens pitch ($p_l = 125$ μ

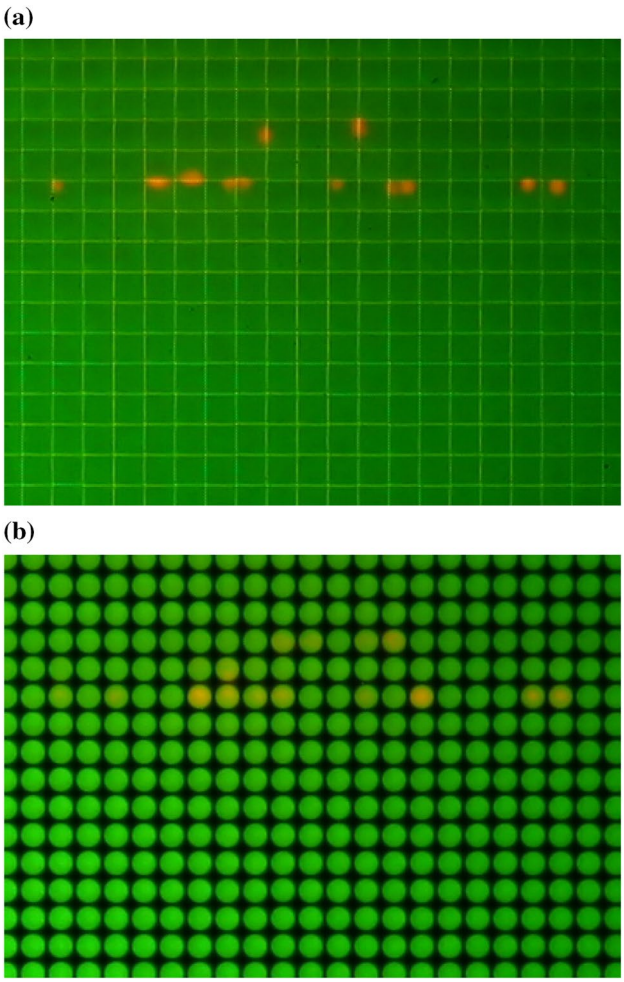

Fig. 5 Images depicting the LF microscope calibration procedure. **a** When the camera focal plane is conjugate with the lenslet array plane, a superimposed grid is visible. **b** When the camera is focused on the back focal plane of the microlens array, subimages are uniformly colored for in-focus objects. The fluorescent particles in this image are in focus

m), the lateral scale of refocused images is computed as $p_l/M = 6.25$ µm/pixel. This scale was applied for all results presented herein; however, we note that the index of refraction difference between air and the working fluid results in a slight reduction of the lateral scale of refocused images. This was quantified in a separate calibration procedure in which a calibration grid was placed in a water-filled volume located in the object space of the actual experiment. A light field image of the grid was refocused and the lateral scale established by measuring the mean distance between reference markers. For the present experimental setup, the actual mean lateral scale of refocused images was found to be 6.05 µm/voxel. Ignoring this correction results in a 3% bias error in the reported velocity components.

The refocused images are assembled into a focal stack and subjected to 3D deconvolution. In ensuing figures, the results from PIV processing of these volumes are labeled 'PIV-1'. However, as evidenced in Fig. 3, the particles are still elongated in the axial dimension even following deconvolution. To assess and mitigate the error this effect introduces into the PIV correlations, we find the centroids of individual particles using a Matlab labeling algorithm, and then replace each particle with a symmetric 3D Gaussian intensity distribution with a particle diameter of 3 voxels. The results from PIV processing of these volumes with synthetic particles replacing the elongated particles are labeled 'PIV-2'. Figure 6 shows an example of the results of this volume reconstruction for one time step in the backward-facing-step microchannel. The red lines denote the channel boundaries and step location. The particle concentration is larger in the middle channel depths and sparser near the top and bottom boundaries. The refocusing and deconvolution algorithms were implemented in Matlab and code and example files are posted online (SplashLab 2014).

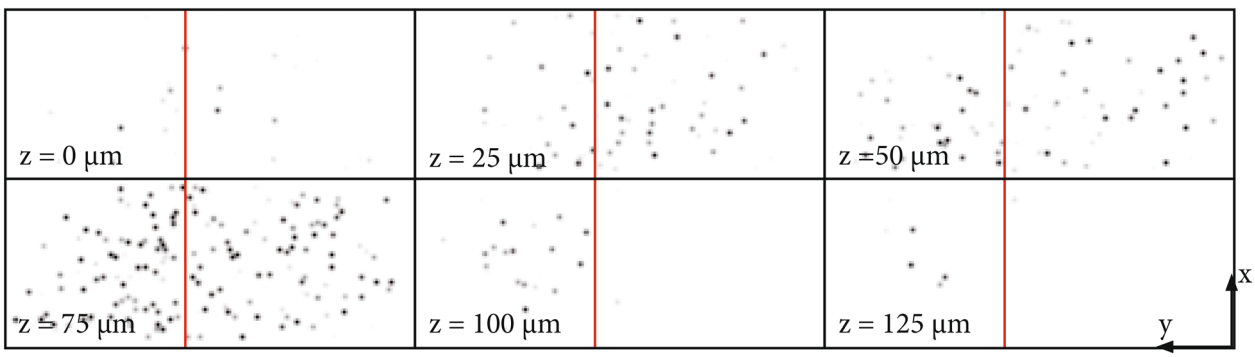

Fig. 6 Slices of a refocused volume at several depth locations throughout the backward-facing-step microchannel at a single time instant. The refocused volume has been deconvolved and particles replaced with symmetric 3D intensity shapes. The *red lines* denote the step location and the origin of the channel coordinate system is marked in the $Z = 125$ µm plane

3.4 PIV

Vector fields are computed from volumes generated from consecutive times using a basic, open-source PIV code called matpiv (Sveen 2004), which was adapted to perform three-dimensional PIV. The algorithm uses a multi-pass 3D cross-correlation between two intensity fields with overlap between adjacent interrogation volumes. For the 0.4 µL/min experiment, one pass at an initial interrogation volume size of $48 \times 48 \times 16$ voxels and two passes at a final interrogation volume size of $24 \times 24 \times 8$ voxels ($x \times y \times z = 150 \times 150 \times 50\,\mu m$) with 75% overlap were used to process 143 vector fields. On average, each $24 \times 24 \times 8$ voxel interrogation volume contained approximately 8 particles.

For the 0.6 µL/min case, 200 vector fields were computed using an initial interrogation volume size of $96 \times 96 \times 16$ voxels and two passes at a final interrogation volume size of $48 \times 48 \times 8$ voxels ($x \times y \times z = 300 \times 300 \times 50\,\mu m$) with 75% overlap. The larger lateral dimension of the interrogation volume was required to accommodate larger particle motions; this is a limitation imposed by the camera frame rate. After the final pass, vectors outside of the channel are set to zero. The fields are then post-processed using a filter based on the signal-to-noise ratio of the cross-correlation peak, a global filter that removes vectors that deviate by more than five standard deviations above the mean of all vectors, and a local filter that removes vectors that deviate by more than three standard deviations from the median of a $3 \times 3 \times 3$ vector window. The filtered fields are then interpolated using linear interpolation, vectors outside of the channel are again set to zero, and finally, the fields are smoothed with a $3 \times 3 \times 3$ Gaussian filter.

3.5 Numerical simulations

To quantify the performance of the light field μPIV method, numerical computational fluid dynamics (CFD) simulations of the channel flow were performed. The model used in the simulation was a half channel with a plane of symmetry to reduce computational time. The width was 207.5 µm, with a thin section height of 75 µm and a thick section height of 145 µm, which is the same as the experimental section. The mesh was composed of hexahedral cells with a near wall prism layer. The boundary conditions consisted of a mass flow inlet, and a split outflow at the outlet; a no-slip boundary condition was imposed at the wall. As the entry length for these Reynolds numbers would be on the order of 1 µm and the length of the experimental channel before the test section is several orders of magnitude larger than this, the inlet flow of the CFD simulation was imposed as fully developed. The flow rate at the inlet corresponded to the volume flow rate of the syringe pump used for the two experimental cases.

4 Results and discussion

Figure 7 shows the velocity field resulting from averaging all 143 vector field image sets measured for the 0.4 µL/min case, with several vectors removed for clarity. For this experiment, the y direction (v velocity) corresponds to the flow-wise direction, the z direction (w velocity) is the axial direction and the x direction (v velocity) is the transverse direction. The vectors are color-coded based on their velocity magnitude. Qualitatively, the results are as expected: a profile is clearly visible from top to bottom and side to side, and velocities in the thin section are higher than velocities in the thick section.

A more quantitative picture is presented in Fig. 8, which shows the evolution of the v velocity profile from the thin to thick section of the channel for both experimental flow rates. Profiles from the PIV data are shown in red (PIV-1) and black (PIV-2) with the horizontal lines indicating one standard deviation from the mean. The blue profiles are from the CFD simulation. The y–z profiles are on the plane $x = 187.5\,\mu m$ and the y–x profiles are on the plane $z = 43.9\,\mu m$. Overall, the PIV performs quite well in capturing the flow velocities, particularly in the thick channel section. The agreement breaks down near the channel boundaries likely due to inhomogenous seeding (Kähler et al. 2012). In addition, the large gradients near the wall—between $x = 0$ and $x = 75\,\mu m$ in the y–x planes, for example—occur on a scale smaller than the interrogation volume dimension. This error near the boundaries is reduced somewhat by replacing the

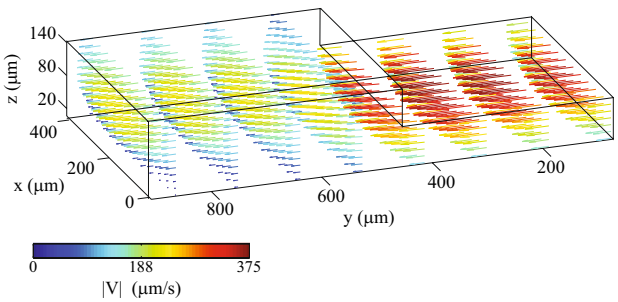

Fig. 7 Experimental vector field of the microchannel flow from the 0.4 µL/min case (PIV-2 processing). A *box* is drawn around the field to indicate the walls of the channel. In this coordinate system, y is the flow-wise direction, z is the axial direction, and x is the transverse direction. Vector *color* represents the velocity magnitude

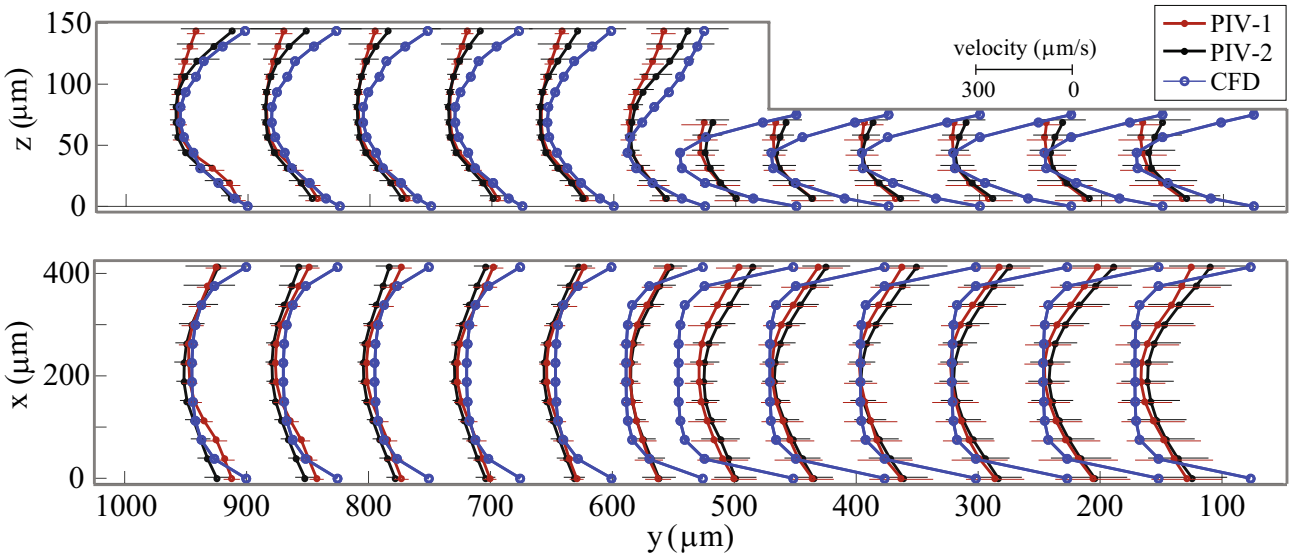

Fig. 8 Comparison of CFD and average PIV velocity profiles showing the development of the flow throughout the channel for the 0.4 μL/min case. The y–z profiles are on the plane $x = 187.5$ μm and the y–x profiles are on the plane $z = 43.9$ μm. The overall agreement between the PIV and CFD is good, but the error at the boundaries is clearly visible in these figures. The *error bars* on the results from each processing approach (PIV-1 and PIV-2) represent one standard deviation from the mean

elongated particles with symmetric particles (PIV-2), but is still large in the small channel section. In addition, by overlapping the interrogation volumes, some of this gradient is captured but is greatly smoothed. Aside from the regions with very large spatial gradients, the velocity deviations from CFD measurements are small. This indicates that the method affords sufficient particle seeding concentration to resolve velocity fields.

The measurement deviation from the numerical simulation is calculated as

$$v_e = \frac{v_{CFD} - \bar{v}_{PIV}}{v_{CFD}} \times 100, \tag{10}$$

where v_{CFD} are the v component velocities predicted by the CFD simulation and $\bar{v}_{PIV}$ are mean velocities measured from PIV. Figure 9 shows contours of v_e on y–z planes across the channel for the 0.4 μL/min case. Confirming the trend shown in Fig. 8, the deviation is typically less than 5% except near the boundaries and near the corner of the backward-facing step. In addition, the error near the top wall of the channel, both in the thin and thick section, is larger than near the bottom wall.

To assess the differences in the w velocity measurements, y–z planes taken at $x = 187.5$ μm are shown for PIV and CFD data in Fig. 10a, b, respectively. While the v velocities appear similar throughout the channel, the PIV significantly underestimates the w velocities near the step. This is clearly shown in Fig. 10c, which plots the w component of velocity at $x = 187.5$ μm and $y = 487.5$ μm, just downstream of the step (location shown by the vertical red lines in Fig. 10a, b).

We now offer some explanations for the differences observed in Figs. 9 and 10. First, as already mentioned, in some places, the spatial gradients are large relative to the interrogation volume size. Also, it is a well-known issue in μPIV that shear can cause particles to migrate away from boundaries (Lindken et al. 2009) causing there to be poor seeding concentration near walls. This effect is mitigated somewhat at the bottom of the channels because particles have settled on the bottom due to gravity over the course of experiments and, thus, contribute to the cross-correlation. These error sources are common to 3D μPIV. An error source that stems from the light field method is the limited axial resolution available; i.e., limited number of distinct depths that can be refocused. This results in a large axial dimension of the interrogation volume relative to the total axial dimension of the measurement volume. As a consequence, large axial gradients in the flow tend to get artificially lessened, as evidenced by the profiles in the thin channel section of Fig. 8. Furthermore, the axial dimension of reconstructed particles is large. Even though the particles have been replaced with symmetric Gaussian intensity distributions, the particle diameter is still large compared to the axial dimension of an interrogation volume. Thus, the accuracy in resolving particle motions in the axial dimension is poor. This accuracy could be improved by using larger axial dimensions of the interrogation volumes at the cost of spatial resolution in the z dimension. This trade-off is driven by the balance between particle depth of focus

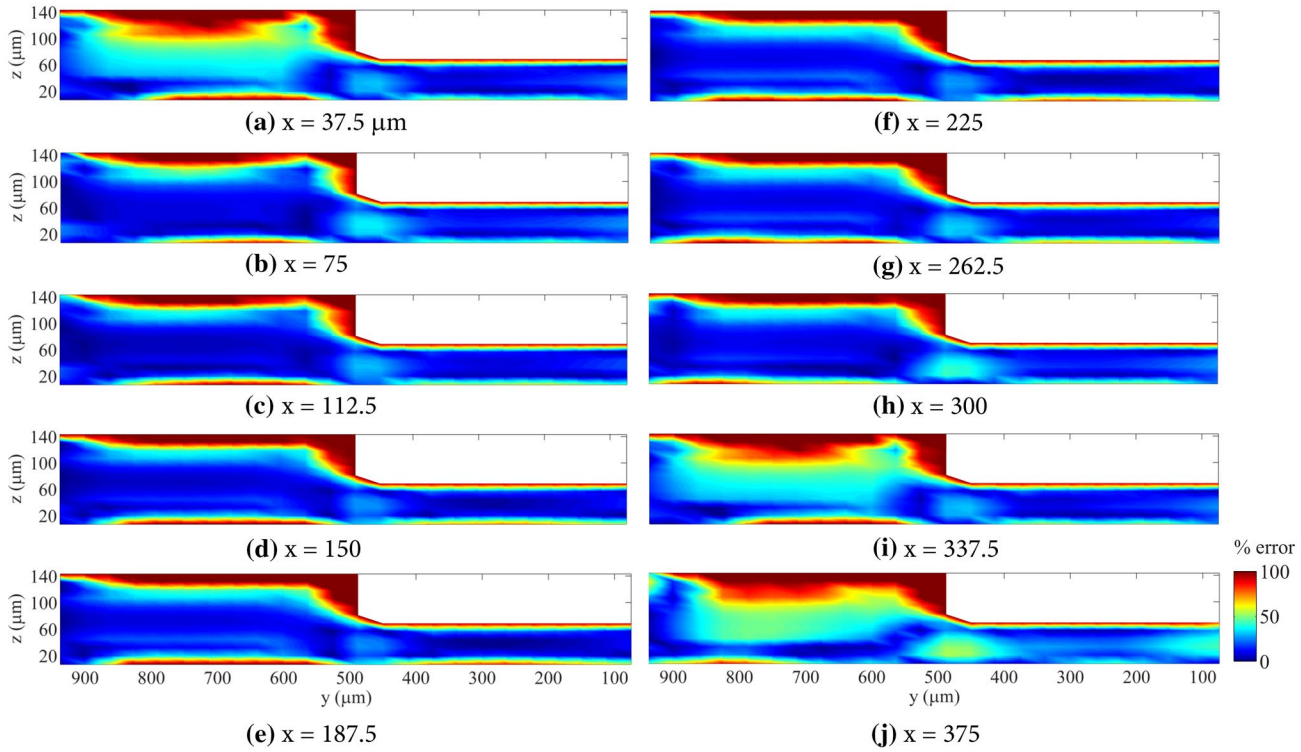

Fig. 9 Slices at several y–z planes showing the error in the v velocity between the average PIV-2 measurements and the CFD simulations for an inlet flow rate of 0.4 µL/min. The x value indicates the distance from the side wall. The error is largest near the step ($y \approx 490$ µm) and at the walls farthest from the objective ($z \approx 140$ µm)

(D_{tot_2}, Eq. 5) and total resolvable depth (D_V, Eq. 6). The total resolvable depth can be increased by increasing lenslet pitch, p_l, to increase the number of resolvable spots, N_u, but this comes at the expense of lateral resolution.

Finally, Table 1 summarizes characteristics of several μPIV and μPTV measurement methods, adding several specifications to a table reported in Tien et al. (2014). The term $\Delta z/\Delta x$ is intended to indicate the spatial resolution in the axial dimension compared to the lateral dimension. For the present work and references Sheng et al. (2006), Ooms et al. (2009), Kim et al. (2012), $\Delta z/\Delta x$ is the ratio of the particle depth of focus to the particle image diameter. For reference Pereira et al. (2007), $\Delta z/\Delta x$ is estimated from the reported sensitivity of the pinhole pattern size to changes in particle depth. Finally, for reference Tien et al. (2014), we estimate $\Delta z/\Delta x$ from the ratio of RMS uncertainties from a ground truth position measurement. All reported techniques exhibit a value of $\Delta z/\Delta x \approx O(5)$, with the exception of one of the pinhole pattern PTV methods (Pereira et al. 2007).

Table 1 also reports N, which is either the number of particles per image or number of vectors per image pair (the latter is reported in parentheses). The final two columns show the number of particles (or vectors) per µm^3 and per total number of useful pixels, respectively. Both are reported relative to the values computed for the present study. The largest seeding concentration is achieved in stereo-micro-PIV, where the relative depth dimension of the volume is small, and in the Tomo-PIV experiment, which is performed with a rather small magnification. With the exception of the diffraction ring method, all other techniques demonstrate comparable particle seeding densities.

5 Conclusions

A method based on light field microscopy for measuring the 2C-3D velocity field of flow through a microchannel was presented. Based on an experimental assessment of light field μPIV and comparison with CFD results, the technique is well suited to accurately measure in-plane (i.e., u, v) velocity components throughout a 3D volume. The technique suffers from limitations on near wall measurement accuracy that are common to 3D μPIV techniques, but the major limitation of the light field μPIV method is the poor axial velocity accuracy stemming from inherent limitations on axial resolution. However, because the 3D positions of particles are reconstructed, the method could be used with a particle tracking velocimetry (PTV) algorithm to resolve 3C-3D velocity fields; this was not performed in the present study due to limitations on the

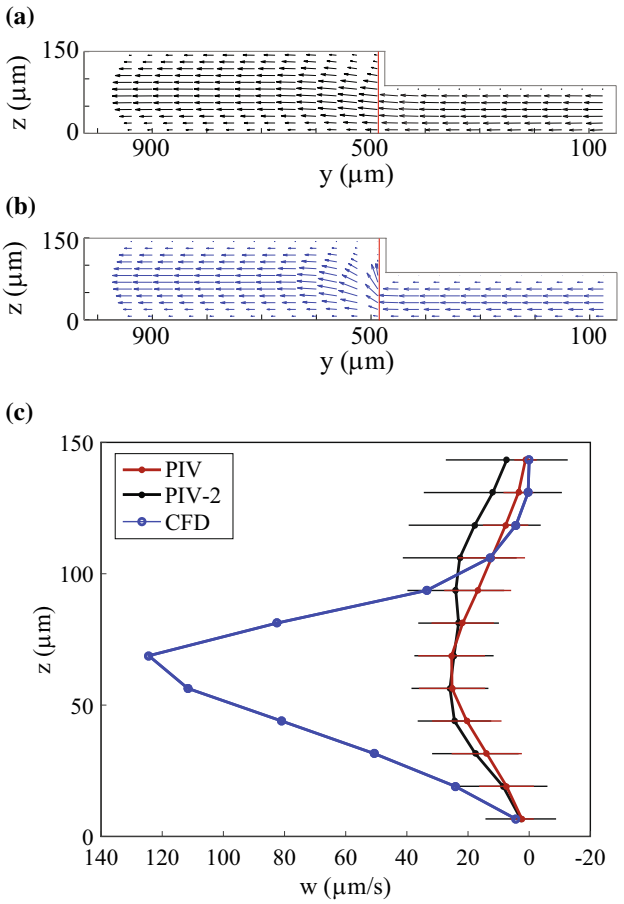

Fig. 10 Comparison of the **a** PIV-2 velocity data and **b** CFD velocity field each at a y–z slice at $x = 187.5$ (only v and w velocity components are plotted). **c** A *line* plot comparing the w velocity of the PIV-1, PIV-2 and CFD. The location of the velocity measurements in **c** is shown by the *vertical red lines* in **a** and **b**. The numerical simulation predicts high velocities at this point reaching roughly 120 μm/s. The PIV, however, significantly underestimates this value by nearly one order of magnitude

frame rate of the camera. Nonetheless, the setup is simple and inexpensive (requiring only the addition of a microlens array) and can be applied to an existing system without modifying the microscope. Overall, light field μPIV provides an attractive option when simple, cost-effective microscopic flow measurements are required.

Acknowledgements This material is based upon work supported by the National Science Foundation under Grant No. 1126862. JB gratefully acknowledges funding from the Office of Naval Research under task number N0001413WX20545 monitored by program officer Dr. Ronald Joslin (ONR Code 333).

Appendix

We now derive the relationship between the synthetic image plane displacement, d and the corresponding object plane displacement, δ, as given by Eq. 2 and shown schematically in Fig. 1a. The object plane is located at a distance

$$s_o^o = \delta + f_o \tag{11}$$

to the left of the objective. The location of the image formed by the objective is found using the thin lens equation to give

$$s_i^o = \frac{f_o s_o^o}{s_o^o - f_o}, \tag{12}$$

where s_i^o is positive to the right of the objective as drawn in Fig. 1a. The image formed by the objective becomes the object for the tube lens and is at a distance

$$\begin{aligned} s_o^t &= f_t + f_o - s_i^o \\ &= f_t + f_o - \frac{f_o s_o^o}{s_o^o - f_o} \end{aligned} \tag{13}$$

Table 1 Summary of characteristics of several μPIV and μPTV measurement methods from Tien et al. (2014) with additional information

Technique (References)	# cameras/# light sources	Volume (μm^3)	M	$\Delta z/\Delta x$	N	N/μm^3, relative	N/pixel, relative
Stereo-micro-PIV (Bown et al. 2006)	2/1	900 × 720 × 45	10×	N/A	12,500	79	138
Diffraction Ring PTV (Peterson et al. 2008)	1/1	222 × 168 × 50	4×	N/A	2.25	0.22	0.023
Digital Holographic PTV (Sheng et al. 2006)	1/1	1500 × 1500 × 1000	10×	7.6	5679	0.47	19.6
Digital Holographic PTV (Ooms et al. 2009)	1/1	1520 × 1520 × 1000	10×	7.5	(367)	0.03	1.27
Pinhole Pattern PTV (Pereira et al. 2007)	1/1	400 × 300 × 160	20×	1.14	N/A	N/A	N/A
Pinhole Pattern PTV (Tien et al. 2014)	1/3	600 × 600 × 600	10×	5.06	(400)	0.34	5.52
Tomo-PIV (Kim et al. 2012)	4/1	2500 × 2100 × 400	1.5×	6	47906	4.21	121
Wavefront Sensing PTV (Chen et al. 2009)	1/1	1830 × 1200 × 500	4×	N/A	(400)	0.07	3.99
Astigmatism PTV (Cierpka et al. 2010)	1/1	500 × 600 × 90	20×	N/A	450	2.71	4.55
Present work	1/1	890 × 425 × 150	20×	4	307	–	–

M is the magnification. $\Delta z/\Delta x$ is the ratio of particle depth of focus to the particle image diameter. N is the number of particles per image (number of vectors per image pair are in parenthesis where appropriate). The number of particles or vectors per μm^3 and the number of particles or vectors per pixel are compared with respect to the present study

from the tube lens (s_o^t is positive to the left of the tube lens). The thin lens equation is then applied to the tube lens to give the distance to the image plane, which coincides with the displaced $s't'$ plane,

$$s_i^t = \frac{f_t\left(\frac{-f_o^2}{s_o^o - f_o}\right) + f_t^2}{\frac{-f_o^2}{s_o^o - f_o}} \tag{14}$$

Inserting the relation for object plane displacement given in Eq. 11, Eq. 14 can be solved to give

$$\begin{aligned} s_i^t =& f_t - \left(\frac{f_t^2}{f_o^2}\right)\delta \\ =& f_t - M^2\delta, \end{aligned} \tag{15}$$

where the definition for magnification has been inserted. Finally, inserting the relation $s_i^t = f_t - d$ into Eq. 15 and rearranging yields,

$$\delta = \frac{d}{M^2} \tag{16}$$

As described in Sect. 2.1, the object plane displacements must be corrected to account for the fact that the index of refraction of the object medium differs from the medium in which the objective is immersed. Pereira and Gharib (2002) derived the correction for the apparent object depth Z, measured from the objective lens plane to the location at which the object would exist if there were no index of refraction changes. The actual object depth is given by

$$Z' = D + w + \Omega\left(n_f\right)\left[Z - D - \frac{w}{\Omega\left(n_w\right)}\right], \tag{17}$$

where D is the distance from the objective plane to the channel wall, w is the thickness of the channel wall, n_w is the index of refraction of the channel wall and the function $\Omega(\nu)$ is defined as

$$\Omega(\nu) = \sqrt{\frac{R^2}{Z^2}\left[\left(\frac{\nu}{n}\right)^2 - 1\right] + \left(\frac{\nu}{n}\right)^2} \tag{18}$$

where $R^2 = X^2 + Y^2$ is the radial coordinate of the object point with respect to the main optical axis and n is the index of refraction of the medium in which the objective is immersed ($n = 1$ herein). For rather extreme values in our setup of $R = 400\,\mu\text{m}$ and $Z = 1000\,\mu\text{m}$, we have $\Omega(n_f) = 1.353$, which is approximately equal to $n_f/n = 1.333$. Therefore, we make an approximation that is often made (Tien et al. 2008; Galbraith 1955) and assume that $\Omega(n_f) \approx n_f/n$, which conveniently removes the dependence of the depth correction on the radial coordinate. Thus, Eq. 17 reduces to

$$Z' = \frac{n_f}{n}Z + \left(1 - \frac{n_f}{n}\right)D + \left(1 - \frac{n_f}{n_w}\right)w \tag{19}$$

where we have also assumed that $\Omega\left(n_w\right) \approx n_w/n$. Therefore, the actual corrected depth distance between any two planes is given as:

$$\Delta Z' = Z_2' - Z_1' = \frac{n_f}{n}\left(Z_2 - Z_1\right) = \frac{n_f}{n}\Delta Z \tag{20}$$

Substituting for ΔZ the apparent object plane displacement δ, we get

$$\delta' = \frac{n_f}{n}\delta \tag{21}$$

which is Eq. 8.

References

Belden J, Pendlebury J, Jafek A, Truscott TT (2014) Advances in light field imaging for measurement of fluid mechanical systems. Dynamic data-driven environmental systems science (DyDESS) conference

Belden J, Truscott TT, Axiak MC, Techet AH (2010) Three-dimensional synthetic aperture particle image velocimetry. Meas Sci Technol 21:125403

Bown MR, MacInnes JM, Allen RWK, Zimmerman WBJ (2006) Three-dimensional, three-component velocity measurements using stereoscopic micro-piv and ptv. Meas Sci Technol 17:2175–2185

Chen S, Angarita-Jaimes N, Angarita-Jaimes D, Pelc B, Greenaway AH, Towers CE, Lin D, Towers DP (2009) Wavefront sensing for three-component three-dimensional flow velocimetry in microfluidics. Exp Fluids 47(4–5):849–863

Cierpka C, Segura R, Hain R, Kähler C (2010) A simple single camera 3c3d velocity measurement technique without errors due to depth of correlation and spatial averaging for microfluidics. Meas Sci Technol 21(4):045401

Cierpka C, Kaehler CJ (2012) Particle imaging techniques for volumetric three-component (3d3c) velocity measurements in microfluidics. J Vis 15:1–31

Elsinga GE, Scarano F, Wieneke B (2006) Tomographic particle image velocimetry. Exp Fluids 41(6):933–947

Fouras A, Jacono DL, Nguyen CV, Hourigan K (2009) Volumetric correlation piv: a new technique for 3d velocity vector field measurement. Exp Fluids 47:569

Galbraith W (1955) The optical measurement of depth. Q J Microsc Sci 3(35):285–288

Kähler CJ, Scharnowski S, Cierpka C (2012) On the uncertainty of digital piv and ptv near walls. Exp Fluids 52:1641–1656

Kim H, Grosse S, Elsinga G, Westerweel J (2011) Full 3d–3c velocity measurement inside a liquid immersion droplet. Exp Fluids 51:395–405

Kim H, Westerweel J, Elsinga GE (2012) Comparison of tomo-piv and 3d-ptv for microfluidic flows. Meas Sci Technol 24(2):024007

Levoy M (2006) Light fields and computational imaging. IEEE Comput 39(8):46–55

Levoy M, Hanrahan P (1996) Light field rendering. ACM SIGGRAPH, pp 31–42

Levoy M, Ng R, Adams A, Footer M, Horowitz M (2006) Light field microscopy. ACM Trans Graph 25(3):924–934

Lima R, Wada S, Tanaka S, Takeda M, Ishikawa T, Tsubota KI, Imai Y, Yamaguchi T (2007) In vitro blood flow in a rectangular pdms microchannel: experimental observations using a confocal micro-piv system. Biomed Microdev 10(2):153–167

Lindken R, Westerweel J, Wieneke B (2006) Stereoscopic micro particle image velocimetry. Exp Fluids 41:161–171

Lindken R, Rossi M, Grosse S, Westerweel J (2009) Micro-particle image velocimetry: recent developments, applications, and guidlines. Lab Chip 9:2551–2567

Lynch K (2011) Development of a 3-d fluid velocimetry technique based on light field imaging. Master's thesis, Auburn University

Lynch K, Fahringer T, Thurow B (2012) Three-dimensional particle image velocimetry using a plenoptic camera. In: 50th AIAA Aerospace Sciences Meeting. Nashville, TN

Ng R, Levoy M, Bredif M, Duval G, Horowitz M, Hanrahan P (2005) Light field photography with a hand-held plenoptic camera. Stanford Tech Report

Ooms T, Lindken R, Westerweel J (2009) Digital holographic microscopy applied to measurement of a flow in a t-shaped micromixer. Exp Fluids 47(6):941–955

Park JS, Choi CK, Kihm KD (2004) Optically sliced micro-piv using confocal laser scanning microscopy (clsm). Exp Fluids 37:105–119

Pereira F, Gharib M (2002) Defocusing digital particle image velocimetry and the three-dimensional characterization of two-phase flows. Meas Sci Technol 13(5):683

Pereira F, Gharib M, Dabiri D, Modarress D (2000) Defocusing digital particle image velocimetry: a 3-component 3-dimensional dpiv measurement technique. Application to bubbly flows. Exp Fluids 29(1):S078–S084

Pereira F, Lu J, Castano-Graff E, Gharib M (2007) Microscale 3d flow mapping with μddpiv. Exp fluids 42(4):589–599

Peterson SD, Chuang H-S, Wereley ST (2008) Three-dimensional particle tracking using micro-particle image velocimetry hardware. Meas Sci Technol 19(11):115406

Sveen KJ (2004) An introduction to MatPIV v.1.6.1 Preprint series. Mechanics and Applied Mathematics

Sheng J, Malkiel E, Katz J (2006) Digital holographic microscope for measuring three-dimensional particle distributions and motions. Appl Opt 45(16):3893–3901

Sibarita J-B (2005) Deconvolution microscopy. Adv Biochem Eng/Biotechnol 95:1288–1292

SplashLab (2014) Synthetic aperture imaging. http://saimaging.org

Tien W-H, Kartes P, Yamasaki T, Dabiri D (2008) A color-coded backlighted defocusing digital particle image velocimetry system. Exp Fluids 44(6):1015–1026

Tien W-H, Dabiri D, Hove JR (2014) Color-coded three-dimensional micro particle tracking velocimetry and application to micro backward-facing step flows. Exp Fluids 55(3):1–14

Yoon SY, Kim KC (2006) 3d particle position and 3d velocity field measurement in a microvolume via the defocusing concept. Meas Sci Technol 17:2897

Zhang Z (2010) A practicle introduction to light field microscopy. Computer Graphics Laboratory. Electrical Engineering, Stanford University, pp 1–15